Korean J. Chem. Eng., 40(11), 2632-2645 (2023)
DOI: 10.1007/s11814-023-1531-y

pISSN: 0256-1115
eISSN: 1975-7220

Microkinetic study of syngas conversion to dimethyl ether over a bifunctional catalyst: CZA/FER

Jiyeong Cho*, Jongmin Park*, Hyun Seung Jung, Jong Wook Bae**, Jonggeol Na***,†, Won Bo Lee*,†, and Myung-June Park****,†**

*School of Chemical and Biological Engineering, Institute of Chemical Processes, Seoul National University, Gwanak-ro 1, Gwanak-gu, Seoul 08826, Korea
**School of Chemical Engineering, Sungkyunkwan University (SKKU), Suwon 16419, Korea
***Department of Chemical Engineering and Materials Science, Graduate Program in System Health Science and Engineering, Ewha Womans University, Seoul 03760, Korea
****Department of Chemical Engineering, Ajou University, Suwon 16499, Korea
(*Received 17 June 2023 • Revised 7 July 2023 • Accepted 10 July 2023*)

Abstract−Dimethyl ether (DME) is an environmentally friendly fuel and economical compound that can be synthesized through methanol (MeOH) dehydration or direct synthesis from syngas via the water-gas shift reaction. Catalysts such as $Cu/ZnO/Al_2O_3$ (CZA) for syngas conversion to MeOH and ferrierite (FER), a group of zeolites, or γ-Al_2O_3 for MeOH dehydration are necessary for these reactions. A hybrid catalyst, CZA/FER, can be used to directly convert syngas into DME via MeOH. While previous studies have developed kinetic models for these catalytic reaction systems using lumped or microkinetic models, differences in describing elementary reactions have led to variations in detail. In this study, we developed a microkinetic model for DME synthesis from syngas via MeOH over a CZA/FER hybrid bifunctional catalyst. We considered detailed reaction rates and site fractions to determine the dominance of DME synthesis path between the associative and dissociative paths. The model is based on a two-site fraction model for each catalyst, with 28 reactions over CZA and nine reactions over FER. Reaction parameters were determined using transition state theory (TST) and the UBI-QEP method for CZA and the second-order Møller-Plesset perturbation theory (MP2) for FER The pre-exponential factors of Arrhenius rate constants were estimated with experimental data at 250 °C which supported the model's accuracy. Our results show that the associative pathway is dominant for DME synthesis over a CZA/FER hybrid catalyst, which differs from our previous research on microkinetic modeling for MeOH dehydration to DME over an FER zeolite. We also suggest an operating condition range for converting CO_2 in the feed. We compared the relative reaction rates of elementary reactions and site fractions in each catalyst to enhance the understanding of the catalytic reaction system.

Keywords: C1 Chemistry, Dimethyl Ether, Kinetic Modeling, Microkinetics, Hybrid Bifunctional Catalyst

INTRODUCTION

Dimethyl ether (DME) has garnered increasing attention as an environmentally friendly compound which does not contribute to global warming or produce NOx, SOx, or particulate matter (PM). It is an economical alternative fuel to diesel due to its high oxygen content, high cetane number, and lack of C-C bonds. Additionally, DME can be converted into various olefin products as a vital intermediate, making it a promising compound for future use [1,2].

There are two primary methods for synthesizing DME, the first of which involves the dehydration of methanol (MeOH) to produce DME and water, catalyzed by solid acid catalysts such as alumina, silica, or zeolites. The second method involves methane partial oxidation, where methane is oxidized to formaldehyde via MeOH, which is then converted to DME using a catalyst such as copper, silver, or platinum [1]. However, the majority of studies have focused on the dehydration of MeOH as the most effective method for synthesizing DME. The catalysts used for MeOH dehydration are typically acidic and include γ-Al_2O_3, Al_2O_3 with silica/phosphorus, and zeolites [3,4]. This reaction is carried out under low pressure of up to 18 bar and temperatures ranging from 250 to 400 °C, resulting in high selectivity towards DME and low coke formation [5]. Meanwhile, MeOH, which serves as a precursor for DME, is primarily synthesized through the hydrogenation of syngas, a mixture CO, CO_2, and H_2. Commercially, syngas conversion to MeOH is carried out using copper-zinc-aluminum oxide (CZA) or iron-chromium oxide catalysts [6]. Although the CZA catalyst is recognized for its high selectivity, its remarkable activity results in the formation of by-products, such as formaldehyde, formic acid, and formate, alongside CO_2 and H_2O, during the hydrogenation of CO and CO_2 [6-8].

The conversion of syngas to DME using catalytic methods has been extensively studied. The process can be divided into two steps: syngas to MeOH conversion and dehydration. The first step involves CO and CO_2 hydrogenation reactions and water gas shift (WGS) reactions. As the hydrogenation reactions occur widely, the syngas

†To whom correspondence should be addressed.
E-mail: jgna@ewha.ac.kr, wblee@snu.ac.kr, mjpark@ajou.ac.kr

to MeOH conversion generates many intermediates and by-products [6]. The second step involves the product of the first step, i.e., MeOH. Commercial catalysts used for direct synthesis of DME from syngas typically comprise two functionally independent catalysts: Cu or Zn-based catalysts for CO and CO_2 hydrogenation and WGS reaction, and zeolite catalysts, which are known for their high selectivity, stability, and resistance to poisoning [8-11].

The detailed mechanisms of each reaction are as follows. The CO and CO_2 hydrogenation and WGS reactions for synthesizing MeOH from syngas primarily use Cu-based catalysts under gas phase conditions, with the $Cu/ZnO/Al_2O_3$ catalyst, also known as CZA, being the most widely used catalyst. The kinetics of MeOH synthesis in the CZA system have been investigated by many researchers. In particular, Graaf et al. developed a lumped kinetic model for MeOH synthesis using a spinning basket reactor with CZA catalyst and successfully reproduced experimental data for CO and CO_2 hydrogenation at 15-50 bar and 483.15-518.15 K [12-15]. Furthermore, the chemical equilibrium of the WGS reaction in a fixed-bed reactor with CZA catalyst was simulated using the Soave-Redlich-Kwong equation of state at 10-80 bar and 473.15-543.15 K. However, lumped kinetic models are limited in their ability to show the details of the elementary reactions.

Several researchers [1,2,10,16-19] have studied the synthesis processes of MeOH and DME. Their studies can be divided into lumped kinetics or microkinetics. Lumped kinetics is a method of modeling the overall reaction rather than each elementary step reaction, and it is performed by assuming a rate-determining step. In contrast, microkinetic modeling involves modeling all possible elementary step reactions without assuming RDS, and it is usually performed for systems for which there is insufficient information on the catalyst for lumped kinetic modeling. The microkinetic model is used for the purpose of analyzing and understanding the catalyst system [20]. It allows us to take a look at the detailed information about the system such as rate controlling, equilibrated species and dominant surface species, etc. Also, it can be used as a reference model for lumped kinetics, which needs some information for the assumptions to be derived. Several computational methods were used to find thermodynamically favorable reactions from a reaction parameter perspective of an unknown catalytic reaction system. The most favorable reaction was estimated based on the activation energy and Gibbs free energy at each elementary step calculated using *ab initio* quantum chemistry methods such as Density Functional Theory [20,21]. However, there is a limitation to evaluating the kinetically favorable reaction path because the concentration of the reactant, which is an important factor of the reaction kinetic system, was not considered. To solve this problem, various microkinetics with the direct use of the Arrhenius equations were carried out. The microkinetic model is composed of the reaction rate equations of each elementary step using both the activation energy that reflects the thermodynamic effect and the concentration that reflects the kinetic effect. Karakaya et al. [22] introduced the site coverage fraction on the catalytic surface for modeling. Methane dehydroaromatization on Mo/Zeolite catalyst was simulated and analyzed using microkinetic modeling composed of 50 elementary steps. The same research team later performed microkinetic studies on Mo/HZSM-5 catalyst using the site fraction of the Molybdenum site and the zeolite site of the bifunctional catalyst [23]. Similarly, Baz et al. [24] utilized a microkinetic model of the CO electro-oxidation reaction extended to two site types, Pt and alloy, to understand the bifunctional activity of the catalyst. Such research exemplifies microkinetic modeling utilizing reaction kinetic parameters that reflect the thermodynamic effects of each part of the bifunctional catalyst.

The MeOH dehydration over FER consists of approximately ten elementary steps including the two competitive pathways in DME synthesis from MeOH: the associative path and the dissociative path. The associative path involves two MeOH molecules being adsorbed onto the Brønsted acid site of the zeolite, leading to the simultaneous dehydration of MeOH. On the other hand, the dissociative path involves one MeOH molecule replacing the hydrogen of the Brønsted acid site of the zeolite to form a CH_3-Z group, and then sequentially reacting with a second MeOH molecule. There has been a debate over which of these two competitive reaction pathways is the primary one in MeOH dehydration over zeolite. Initially, the γ-Al_2O_3 catalyst was commonly used as an acidic dehydration catalyst. It adsorbs and dehydrates MeOH molecules, and converts them into DME [25]. Aguayo et al. [7] demonstrated a bifunctional catalyst to convert CO, CO_2, and H_2 feed into DME using CZA/γ-Al_2O_3 in 2007. Recently, zeolites have become the preferred catalyst for dehydrating MeOH because of its resistance for deactivation by coke accumulation [5]. Kubelková et al. [26] suggested that MeOH adsorbs to the active site of zeolite when MeOH hydration begins. Blaszkowski and van Santen [27,28] divided the reaction into three pathways, including the associative and dissociative paths at the H-site of zeolite [28]. Based on DFT calculations, they claimed the dominance of the associative path. Conversely, there exists the opposing view that the dissociative path is dominant [17, 29]. Jones and Iglesia [29,30] argued that the dominance of the two paths is not absolute and depends on the conditions, particularly at high temperature and low pressure where the dissociative path is dominant. Similarly, Moses and Nørskov [17] claimed the dominance of the dissociative path based on DFT and relative reaction rate calculations. However, Carr et al. [31], based on reaction kinetic measurement and DFT calculations at 433 K, argued that medium and large size zeolites are not inhibited in high-pressure conditions, while small-pore zeolites are inhibited in dehydration to DME, due to the clustering effect of MeOH. Di Iorio et al. [2] studied the inhibition of MeOH dehydration to DME for zeolites with different pore sizes in high-pressure conditions where the partial pressure of MeOH is above 10 kPa and claimed that the associative path is thermodynamically dominant at high MeOH partial pressures due to the conjugation stabilization effect of MeOH. Generally, it is known that the dissociative path is dominant at temperatures above 500 K and pressures below 10 kPa, while the associative path is dominant at relatively low temperatures below 500 K and pressures above 10 kPa. However, it can vary depending on the specific conditions of the reaction system. In Fig. 1, a scheme of the disputed associative and dissociative reactions is illustrated.

In summary, although the FER system comprises a relatively small number of reactions, microkinetic analysis can still be applied to the CZA system since it contains a significant number of possible elementary-step reactions. There were some earlier studies that construct the kinetic model of the bifunctional catalyst with two

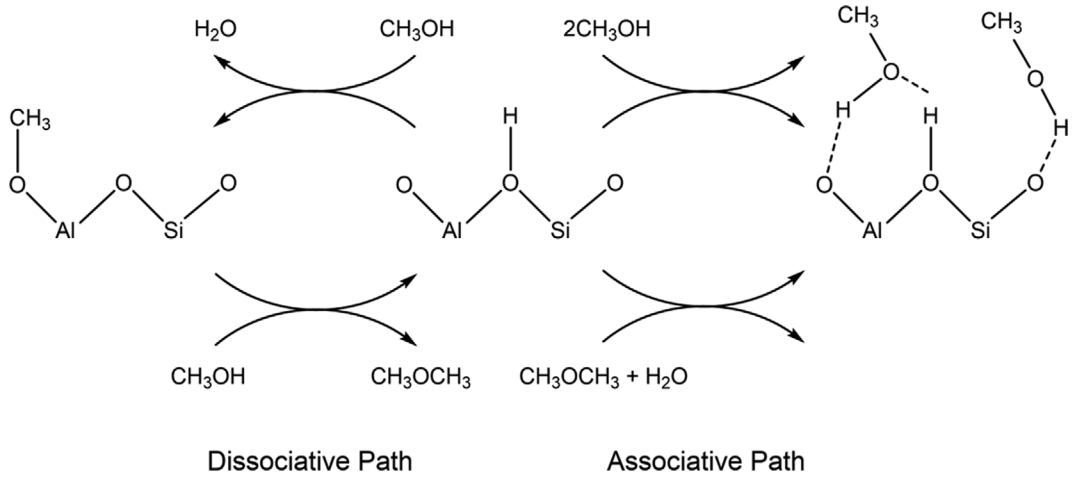

Fig. 1. Dissociative (left) and associative (right) paths for MeOH dehydration.

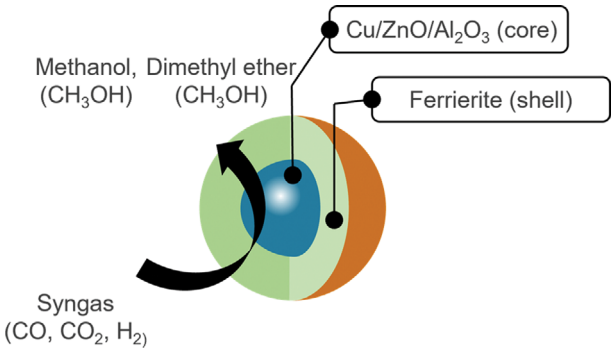

Fig. 2. Dissociative (left) and associative (right) paths for MeOH dehydration.

different active sites for each reactant [7,10]. However, no studies have been conducted on the microkinetic modeling of the CZA/FER hybrid bifunctional catalyst, which has been developed using the core-shell structure described in Fig. 2 below. The microkinetic modeling for bifunctional catalysts can provide a variety of information about CZA/FER system and can compare those with the previous results of CZA [32] and FER [19] each. In this study, a microkinetic model for the CZA/FER hybrid bifunctional catalytic system is developed to investigate how the disputed HCOO** and COOH* intermediates in the CZA system affect the reaction patterns, how the CO_2 conversion differs depending on the hydrogen ratio in the feed and which elementary-step reactions are influenced by it, and how the competition between the associative and dissociative paths in the FER system changes.

METHODS

1. Microkinetic Modeling

The microkinetic model comprises 28 reactions over CZA and nine reactions over FER. The CZA reactions include six adsorption/desorption reactions, while the FER reactions include three adsorption/desorption reactions. The remaining reactions in both cases are surface reactions. The rate equations for each type of reaction are provided below.

Adsorption reactions

$$r_i = k_i * \theta_{vacant} * P_i,\ k = A \quad (1)$$

Desorption reactions

$$r_i = k_i * \theta_i,\ k = A \quad (2)$$

Surface reactions

$$r_i = k_i * \theta_i,\ k = S_{c,i} * e^{\frac{-E_{a,i}}{RT}} \quad (3)$$

Chemical master equation

$$\frac{dy_i}{dt} = \frac{y_{i-1} - y_i}{\tau} + \sum_j r_j \dot{v},\ \frac{dy_i}{dt} \to 0 \quad (4)$$

θ_i, which represents the surface coverage for species i, were designated in each CZA and FER individually, and the site balance was constructed to satisfy $\Sigma\theta_{i,CZA}=1$ and $\Sigma\theta_{i,FER}=1$.

The reaction mechanism for DME synthesis from syngas via MeOH consists of the following overall reactions:

CO hydrogenation

$$CO(g)+2H_2(g) \leftrightarrow CH_3OH(g) \quad (5)$$

CO_2 hydrogenation

$$CO_2(g)+3H_2(g) \leftrightarrow CH_3OH(g)+H_2O(g) \quad (6)$$

WGS reaction

$$H_2O(g)+CO(g) \leftrightarrow H_2(g)+CO_2(g) \quad (7)$$

MeOH dehydration

$$2CH_3OH(g) \leftrightarrow CH_3OCH_3(g)+H_2O(g) \quad (8)$$

The first three reactions produce MeOH from syngas over CZA, and Grabow et al. [6] proposed 49 elementary reactions for the production of the adsorbed form of MeOH, CH_3OH*, including the formation of other possible hydrogenated compounds such as HCO*, HCOO**, CH_2O*, COOH*, H_2COO*, CH_3O*, CH_3OO*,

Table 1. Elementary step reactions for the syngas conversion to DME over a CZA/FER hybrid catalytic system [19,32]

No.	Reaction	r_f	r_b	Reaction type
R1	$CO+*\leftrightarrow CO*$	$r_{f1}P_{CO}\theta_{Cu}$	$r_{b1}\theta_{CO}$	Adsorption /desorption reactions over a CZA
R2	$CO_2+*\leftrightarrow CO_2*$	$r_{f2}P_{CO_2}\theta_{Cu}$	$r_{b2}\theta_{CO_2}$	
R3	$H_2+2*\leftrightarrow 2H*$	$r_{f3}P_{H_2}\theta_{Cu}$	$r_{b3}\theta_{H_2}$	
R4	$H_2O+*\leftrightarrow H_2O*$	$r_{f4}P_{H_2O}\theta_{Cu}$	$r_{b4}\theta_{H_2O}$	
R5	$CH_2O+*\leftrightarrow CH_2O*$	$r_{f5}P_{CH_2O}\theta_{Cu}$	$r_{b5}\theta_{CH_2O}$	
R6	$CH_3OH+*\leftrightarrow CH_3OH*$	$r_{f6}P_{CH_3OH}\theta_{Cu}$	$r_{b6}\theta_{CH_3OH}$	
R7	$CO*+O*\leftrightarrow CO_2*+*$	$r_{f7}\theta_{CO}\theta_{O}$	$r_{b7}\theta_{CO_2}\theta_{Cu}$	Surface reactions over a CZA
R8	$CO*+OH*\leftrightarrow COOH*+*$	$r_{f8}\theta_{CO}\theta_{OH}$	$r_{b8}\theta_{COOH}\theta_{Cu}$	
R9	$CO_2*+H*\leftrightarrow COOH*+*$	$r_{f9}\theta_{CO_2}\theta_{H}$	$r_{b9}\theta_{COOH}\theta_{OH}$	
R10	$CO_2*+H_2O*\leftrightarrow COOH*+OH*$	$r_{f10}\theta_{CO_2}\theta_{OH}$	$r_{b10}\theta_{COOH}\theta_{OH}$	
R11	$H_2O*+*\leftrightarrow OH*+H*$	$r_{f11}\theta_{H_2O}\theta_{Cu}$	$r_{b11}\theta_{OH}\theta_{H}$	
R12	$OH*+*\leftrightarrow O*+H*$	$r_{f12}\theta_{OH}\theta_{Cu}$	$r_{b12}\theta_{O}\theta_{H}$	
R13	$2OH*\leftrightarrow H_2O*+O*$	$r_{f13}\theta_{OH}^2$	$r_{b13}\theta_{H_2}\theta_{O}$	
R14	$CO_2*+H*\leftrightarrow HCOO**$	$r_{f14}\theta_{CO_2}\theta_{H}$	$r_{b14}\theta_{HCOO}$	
R15	$HCOO**+H*\leftrightarrow H_2COO*+2*$	$r_{f15}\theta_{HCOO}\theta_{H}$	$r_{b15}\theta_{H_2COO}\theta_{Cu}^2$	
R16	$H_2COO*+H*\leftrightarrow CH_3O_2*+*$	$r_{f16}\theta_{H_2COO}\theta_{H}$	$r_{b16}\theta_{CH_3O_2}\theta_{Cu}$	
R17	$H_2COO*+*\leftrightarrow CH_2O*+O*$	$r_{f17}\theta_{H_2COO}\theta_{Cu}$	$r_{b17}\theta_{CH_2O}\theta_{O}$	
R18	$CH_3O_2*+*\leftrightarrow CH_2O*+OH*$	$r_{f18}\theta_{CH_3O_2}\theta_{Cu}$	$r_{b18}\theta_{CH_2O}\theta_{OH}$	
R19	$CH_2O*+H*\leftrightarrow CH_3O*+*$	$r_{f19}\theta_{CH_2O}\theta_{H}$	$r_{b19}\theta_{CH_3O}\theta_{Cu}$	
R20	$CH_3O*+H*\leftrightarrow CH_3OH*+*$	$r_{f20}\theta_{CH_3O}\theta_{H}$	$r_{b20}\theta_{CH_3OH}\theta_{Cu}$	
R21	$CO*+H*\leftrightarrow HCO*+*$	$r_{f21}\theta_{CO}\theta_{H}$	$r_{b21}\theta_{HCO}\theta_{Cu}$	
R22	$HCOO**\leftrightarrow HCO*+O*$	$r_{f22}\theta_{HCOO}$	$r_{b22}\theta_{HCO}\theta_{O}$	
R23	$HCO*+H*\leftrightarrow CH_2O*+*$	$r_{f23}\theta_{HCO}\theta_{H}$	$r_{b23}\theta_{CH_2O}\theta_{Cu}$	
R24	$CO*+OH*\leftrightarrow HCO*+O*$	$r_{f24}\theta_{CO}\theta_{OH}$	$r_{b24}\theta_{HCO}\theta_{O}$	
R25	$CO*+H_2O*\leftrightarrow HCO*+OH*$	$r_{f25}\theta_{CO}\theta_{H_2O}$	$r_{b25}\theta_{HCO}\theta_{OH}$	
R26	$CH_3O*+CO*\leftrightarrow CH_2O*+HCO*$	$r_{f26}\theta_{CH_3O}\theta_{H}$	$r_{b26}\theta_{CH_2O}\theta_{HCO}$	
R27	$CH_3O*+HCO*\leftrightarrow CH_3OH*+CO*$	$r_{f27}\theta_{CH_3O}\theta_{HCO}$	$r_{b27}\theta_{CH_3OH}\theta_{CO}$	
R28	$CH_3O_2*+H*\leftrightarrow CH_2O*+H_2O*$	$r_{f28}\theta_{CH_3O_2}\theta_{H}$	$r_{b28}\theta_{CH_2O}\theta_{H_2O}$	
R29	$CH_3OH\ (g)+HZ\leftrightarrow CH_3OH\text{-}HZ$	$r_{f29}P_{CH_3OH}\theta_{H\text{-}Z}$	$r_{b29}\theta_{CH_3OH\text{-}H\text{-}Z}$	Surface reactions over a FER
R30	$CH_3OH\text{-}HZ\leftrightarrow H_2O\text{-}CH_3\text{-}Z$	$r_{f30}\theta_{CH_3OH\text{-}H\text{-}Z}$	$r_{b30}\theta_{H_2O\text{-}CH_3\text{-}Z}$	
R31	$H_2O\text{-}CH_3\text{-}Z\rightarrow CH_3\text{-}Z+H_2O\ (g)$	$r_{f31}\theta_{H_2O\text{-}CH_3\text{-}Z}$	-	
R32	$CH_3\text{-}Z+CH_3OH\ (g)\leftrightarrow CH_3OH\text{-}CH_3\text{-}Z$	$r_{f32}P_{CH_3OH}\theta_{CH_3\text{-}Z}$	$r_{b32}\theta_{CH_3OH\text{-}CH_3\text{-}Z}$	
R33	$CH_3OH\text{-}CH_3\text{-}Z\leftrightarrow CH_3OCH_3\text{-}HZ$	$r_{f33}\theta_{CH_3OH\text{-}CH_3\text{-}Z}$	$r_{b33}\theta_{CH_3OCH_3\text{-}H\text{-}Z}$	
R34	$CH_3OCH_3\text{-}HZ\leftrightarrow CH_3OCH_3\ (g)+HZ$	$r_{f34}\theta_{CH_3OCH_3\text{-}H\text{-}Z}$	$r_{b34}\theta_{CH_3OCH_3}\theta_{H\text{-}Z}$	
R35	$CH_3OH\text{-}HZ+CH_3OH\ (g)\leftrightarrow CH_3OH\text{-}CH_3OH\text{-}HZ$	$r_{f35}P_{CH_3OH}*\theta_{CH_3OH\text{-}H\text{-}Z}$	$r_{b35}*\theta_{CH_3OH\text{-}CH_3OH\text{-}H\text{-}Z}$	
R36	$CH_3OH\text{-}CH_3OH\text{-}HZ\leftrightarrow CH_3OCH_3\text{-}H_2O\text{-}HZ$	$r_{f36}*\theta_{CH_3OH\text{-}CH_3OH\text{-}H\text{-}Z}$	$r_{b36}*\theta_{CH_3OCH_3\text{-}H_2O\text{-}H\text{-}Z}$	
R37	$CH_3OCH_3\text{-}H_2O\text{-}HZ\rightarrow HZ+CH_3OCH_3\ (g)+H_2O\ (g)$	$r_{f37}*\theta_{CH_3OCH_3\text{-}H_2O\text{-}H\text{-}Z}$	-	

and $HCOOCH_3$*. The reaction system also includes gas-phase species absorbed on the surface such as CO*, CO_2*, H*, H_2O*, OH*, and CH_2O*. 28 elementary-step reactions were selected from these by neglecting undetected gas-phase species like HCOOH(g) and $HCOOCH_3$(g), and their surface intermediates [32] (Reactions 1-28 in Table 1).

The fourth overall reaction, the MeOH dehydration reaction, produces DME over FER, based on the two specific paths: associative and dissociative. Computational chemistry analyses have suggested elementary-step reactions (Reactions 29-37 in Table 1) [17, 19,27,28,30]. Reaction 29 is the adsorption of MeOH to FER and is a starting step for both paths. Reactions 30-34 constitute the dissociative path, with CH_3-Z as an intermediate, whereas reactions 35-37 are the associative path, with CH_3OH-CH_3OH-H-Z as an intermediate.

2. Parameter Derivation for Microkinetic Modeling

2-1. The Arrhenius Equation and Transition State Theory (TST)

The kinetic parameters were calculated in the form of the Arrhenius equation:

$$k_{AB}=A_{AB}*e^{\frac{-E_a}{k_BT}} \tag{9}$$

The pre-exponential factors (A_{AB}) were derived from transition state theory (TST), which provides a qualitative explanation for the

Table 2. Base parameter set of parameter estimation: CZA

Reaction	A_f [s^{-1}]	A_b [s^{-1}]	E_f [eV]	E_b [eV]	Bond index
R1	1.00E+00	1.00E+13	0.00	0.71	0.50
R2	1.00E+00	1.00E+13	0.00	0.04	0.50
R3	1.00E+00	1.00E+13	0.00	0.27	0.50
R4	1.00E+00	1.00E+13	0.00	0.18	0.50
R5	1.00E+00	1.00E+13	0.00	0.06	0.50
R6	1.00E+00	1.00E+13	0.00	0.19	0.50
Reaction	A_f [s^{-1}]	A_b [s^{-1}]	E_f [eV]	E_b [eV]	Bond index
R7	1.00E+13	1.00E+13	1.62	0.53	0.95
R8	1.00E+13	1.00E+13	0.21	0.37	0.50
R9	1.00E+13	1.00E+13	0.00	0.52	0.95
R10	1.00E+13	1.00E+13	0.00	0.78	0.50
R11	1.00E+13	1.00E+13	0.81	0.55	0.50
R12	1.00E+13	1.00E+13	1.17	0.44	0.50
R13	1.00E+13	1.00E+13	0.61	0.14	0.95
R14	1.00E+13	1.00E+13	0.30	0.02	0.50
R15	1.00E+13	1.00E+13	0.20	1.09	0.50
R16	1.00E+13	1.00E+13	1.25	0.64	0.60
R17	1.00E+13	1.00E+13	0.76	0.00	0.50
R18	1.00E+13	1.00E+13	0.65	0.00	0.50
R19	1.00E+13	1.00E+13	0.98	0.01	0.50
R20	1.00E+13	1.00E+13	1.33	1.09	0.95
R21	1.00E+13	1.00E+13	0.00	0.72	0.50
R22	1.00E+13	1.00E+13	2.08	0.00	0.50
R23	1.00E+13	1.00E+13	0.62	0.19	0.50
R24	1.00E+13	1.00E+13	0.00	1.45	0.50
R25	1.00E+13	1.00E+13	0.00	0.98	0.50
R26	1.00E+13	1.00E+13	0.00	1.70	0.50
R27	1.00E+13	1.00E+13	0.00	0.96	0.50
R28	1.00E+13	1.00E+13	0.42	0.03	0.50

Table 3. Base parameter set of parameter estimation: FER

Reaction	A_f [s^{-1}]	A_b [s^{-1}]	E_f [eV]	E_b [eV]
R29	1.00E+13	1.00E+13	0.000	0.751
R32	1.00E+13	1.00E+13	0.000	0.467
R35	1.00E+13	1.00E+13	0.000	0.243
Reaction	A_f [s^{-1}]	A_b [s^{-1}]	E_f [eV]	E_b [eV]
R30	1.00E+13	1.00E+13	2.876	2.769
R31	1.00E+13	1.00E+13	0.374	-
R33	1.00E+13	1.00E+13	2.669	2.914
R34	1.00E+13	1.00E+13	0.705	0.000
R36	1.00E+13	1.00E+13	2.509	2.770
R37	1.00E+13	1.00E+13	0.978	-

relationship between chemical reactions and molecular structures based on collision theory. TST assumes a quasi-equilibrium between reactants, activated complexes, and products. In TST, the kinetic parameter for the forward reaction is related to the equilibrium constant for the formation of the activated complex. Based on TST, the values of A for molecular adsorption and dissociative adsorption were set on the order of 10^1 $Pa^{-1}s^{-1}$, while those for molecular desorption and associative desorption were set on the order of 10^{13} s^{-1}. The initial values for the pre-exponential factors of the Langmuir-Hinshelwood surface reactions were set on the order of 10^{13} s^{-1} as in our previous research [32,33].

2-2. Activation Energy: UBI-QEP Method and MP2 Calculations

The CZA catalytic reaction system consists of 28 reversible reactions, comprising a total of 56 elementary reactions of forward and reverse. Due to the high computational cost associated with performing ab-initio-based activation energy calculations in such a large reaction system, empirical equations such as the unity bond index-quadratic exponential potential (UBI-QEP) have been used in previous research [32,34].

The UBI-QEP method is a semiempirical methodology for calculating the activation energies based simply on the adsorption energy (Q), the enthalpy of the reaction (ΔH_{rxn}), and the bond index (Φ). It assumes that two-body interactions in a multi-body system can be described as a quadratic potential of the exponential function of the two-center bond distance, similar to the bond index. By using this method, activation energies can be calculated

Table 4. Operating conditions of the experiments

Exp	T [°C]	P [bar]	GHSV [L/(kg_{cat} h]	$CO/CO_2/H_2/N_2$ /[vol%]	$H_2/(2CO+3CO_2)$	Remarks
1	250	50	2000	21.0/6.0/66.0/4.0	0.96	Base case
2	250	20	2000	21.0/6.0/66.0/4.0	0.96	
3	250	30	2000	21.0/6.0/66.0/4.0	0.96	Pressure
4	250	40	2000	21.0/6.0/66.0/4.0	0.96	
5	250	50	4000	21.0/6.0/66.0/4.0	0.96	
6	250	50	6000	21.0/6.0/66.0/4.0	0.96	GHSV
7	250	50	8000	21.0/6.0/66.0/4.0	0.96	
8	250	50	2000	15.6/6.4/73.9/4.7	1.50	Feed
9	250	50	2000	11.5/4.9/79.4/4.2	2.10	Composition

using the enthalpies of the gas-species, the adsorption energies of the surface intermediates, and the bond indices of all of these with minimal computational burden [32]. Therefore, the method was applied to calculate the activation energies of the 28 forward and backward reactions over CZA.

In Table 2, the base parameter set over CZA catalyst for parameter estimation has been displayed.

In the FER zeolite system, the activation energy was available in the previous study [19] where the second-order Møller-Plesset perturbation theory (MP2) calculations were applied. MP2 is a calculation methodology that accounts for electron correlation effects, making it well-suited to describe dispersion interactions [35], despite its high computational cost. Since the catalytic transformation of hydrocarbons over zeolites involves bond rearrangements and van-der-Waals interactions, it is important to consider the dispersion interactions of zeolites. To this end, we conducted MP2 calculations for a 4T cluster model of FER in our study [19].

In Table 3, the base parameter set over FER catalyst for parameter estimation has been displayed.

2-3. Parameter Estimation

Parameter estimation was performed using experimental data based on the operation result. The data were obtained from our previous work [10] (Table 4). There was a total of 12 experimental data under various temperatures, pressures, gas hourly space velocities (GHSV), and feed compositions. Among the 12 experimental data, three data for the temperature change were excluded because the activation energies of 72 elementary-step reactions were not estimated. The experimental conditions of the data are described in Table 4.

The production rates of other byproducts like formaldehyde, formic acid, and light hydrocarbons containing methane, ethane, and ethylene were neglected because their carbon-mole% in the experiment were less than 1%.

MATLAB (MathWorks, Inc.) was used as the primary platform, where the stiff ODE solver (ode15s) with the backward differentiation formula (BDF) algorithm was employed to solve the mass balance equations. Parameter estimation was conducted using the genetic algorithm (GA) to minimize the following objective function:

$$F_{obj}=\Sigma_{i=1}^{9}\{WF_1[(X_{CO,\,calc}-X_{CO,\,exp})^2+(X_{CO_2,\,calc}-X_{CO_2,\,exp})^2]+ WF_2[(N_{CH_3OH,\,calc}-N_{CH_3OH,\,exp})^2+(N_{CH_3OCH_3,\,calc}-N_{CH_3OCH_3,\,exp})^2]\} \quad (10)$$

In the above equation, i, X, and N represent each experimental run, conversion, and molar flowrate, respectively, and WF denotes the weighting factor for each objective element.

RESULTS AND DISCUSSION

The estimated values of the pre-exponential factors are listed in Table 5, and comparisons of CO conversion [%], CO_2 conversion [%], MeOH flowrate [mol/s] and DME flowrate [mol/s] between the simulated and experimental values are illustrated in Figs. 3 and 4.

The CO and CO_2 conversions increased with increasing pressure (Exp1-4), while the increase of GHSV resulted in a decrease in conversion (Exp1, 5-7). The effects of hydrogen to carbon ratio (Exp8-9) on CO_2 conversion are particularly remarkable, indicating that CO_2 is consumed under the conditions of high H_2 composition. The simulated values of the four objective elements were normalized using the means and standard deviations of the exper-

Table 5. Estimated parameter set: CZA/FER

Reaction	a [$Pa^{-1}s^{-1}$]		E_f [eV]	E_b [eV]
R1	3.20E-19		0.00	0.71
R2	3.35E-08		0.00	0.04
R3	1.55E-12		0.00	0.27
R4	8.77E-18		0.00	0.18
R5	5.15E-06		0.00	0.06
R6	1.10E-34		0.00	0.19
Reaction	A_f [s^{-1}]	A_b [s^{-1}]	E_f [eV]	E_b [eV]
R7	6.88E+16	1.00E+13	1.62	0.53
R8	1.19E+19	1.00E+13	0.21	0.37
R9	4.14E+06	1.00E+13	0.00	0.52
R10	6.37E+17	1.00E+13	0.00	0.78
R11	6.29E+11	1.00E+13	0.81	0.55
R12	6.85E+17	1.00E+13	1.17	0.44
R13	1.44E+11	1.00E+13	0.61	0.14
R14	4.52E+04	1.00E+13	0.30	0.02
R15	3.20E+18	1.00E+13	0.20	1.09
R16	2.86E+17	1.00E+13	1.25	0.64
R17	1.24E+17	1.00E+13	0.76	0.00
R18	1.25E+13	1.00E+13	0.65	0.00
R19	8.21E+05	1.00E+13	0.98	0.01
R20	1.06E+10	1.00E+13	1.33	1.09
R21	5.20E+07	1.00E+13	0.00	0.72
R22	1.67E+14	1.00E+13	2.08	0.00
R23	1.01E+13	1.00E+13	0.62	0.19
R24	9.38E+12	1.00E+13	0.00	1.45
R25	2.10E+19	1.00E+13	0.00	0.98
R26	7.54E+21	1.00E+13	0.00	1.70
R27	1.16E+06	1.00E+13	0.00	0.96
R28	1.36E+09	1.00E+13	0.42	0.03
Reaction	A_f [$Pa^{-1}s^{-1}$]	A_b [$Pa^{-1}s^{-1}$]	E_f [eV]	E_b [eV]
R29	3.55E+04	1.00E+13	0.000	0.751
R32	1.43E+07	1.00E+13	0.000	0.467
R35	1.00E+11	1.00E+13	0.000	0.243
Reaction	A_f [$Pa^{-1}s^{-1}$]	A_b [$Pa^{-1}s^{-1}$]	E_f [eV]	E_b [eV]
R30	1.00E+14	3.83E+13	2.876	2.769
R31	1.00E+18	-	0.374	-
R33	1.00E+11	3.46E+16	2.669	2.914
R34	1.00E+19	1.57E+03	0.705	0.000
R36	1.00E+22	3.01E+16	2.509	2.770
R37	1.00E+19	-	0.978	-

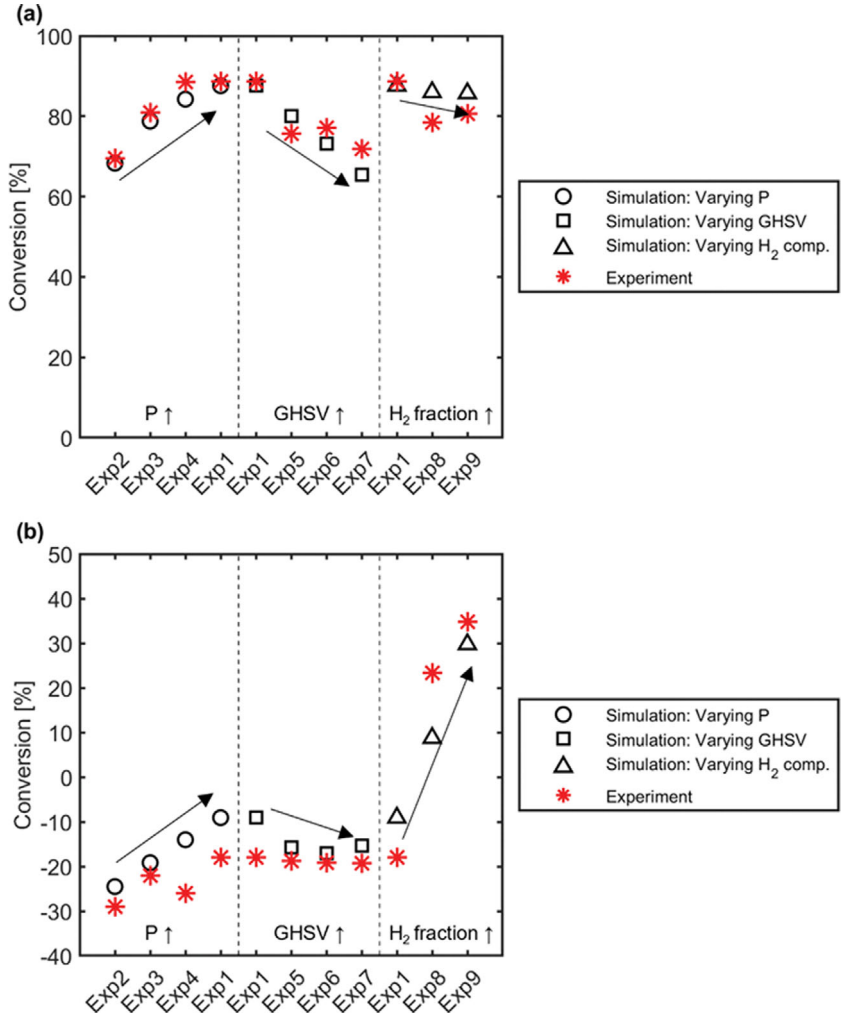

Fig. 3. Comparison of (a) CO conversion [%] and (b) CO_2 conversion [%] between the simulated and experimental values. The arrangement of experiment data in x-axis shows clusters of changing in operating condition.

imental data, and the parity plot between raw data for 36 experimental and simulation data points is presented in the supporting information.

The prediction results of MeOH/DME flow rates reflected the trend of the experimental values. Notably, MeOH production decreased with increasing hydrogen to carbon ratios, whereas DME production increased, indicating an accelerated adsorption reaction and promotion of the transformation to DME. In Fig. 7, the ratio of net reaction rates between Exp9 and Exp1 is presented, indicating that with reaction 6, 29, 32 and 35, adsorption reactions of MeOH to catalyst, increased in Exp9 where the hydrogen to carbon ratio in feed increased than Exp1 where is the base case. However, the model's predicted values did not reflect the trend of experimental values of DME production rate with Exp1 and 8-9, the increasing in hydrogen to carbon ratio. Upon examining the experimental values under the given conditions, the CO conversion remains relatively constant, while the CO_2 conversion is increasing. Although the carbon conversion increases, the experimental data shows decreasing in both MeOH and DME synthesis. It may be the experimental error and the model's results, in which the MeOH production rate decreases and the DME production rate increases with the rise in carbon conversion, can be considered reasonable.

3. Site Fractions

In the case of the CZA catalyst, the criterion of 10^{-7} was used to distinguish major and minor components, resulting in the fractions of CO*, CO_2*, H*, HCOO**, COOH*, and vacant sites to be the major components (Fig. S2 in the Supporting Information). Among the minor components, CH_2O* and CH_3O* showed a relatively important proportion. As HCOO** has been reported as a major component in the literature [6,9,36-38], HCOO** was identified as the major surface component in this work. On the other hand, COOH* which is not a major component in other studies, is one of the major surface components in this study. Moreover, the fraction of HCOO**, CH_2O* and CH_3O* shows significant increase in condition of high H_2 composition in feed condition, Exp8 and Exp9. HCOO** and COOH* are involved in reactions 8, 9, 10, and reactions 14, 15, 22, respectively. In addition, the hydrogenation of HCOO** in reaction 15 is often considered a promising candidate for the rate-determining step (RDS) [9,38] and that pathway is a major part of CO_2 hydrogenation to MeOH.

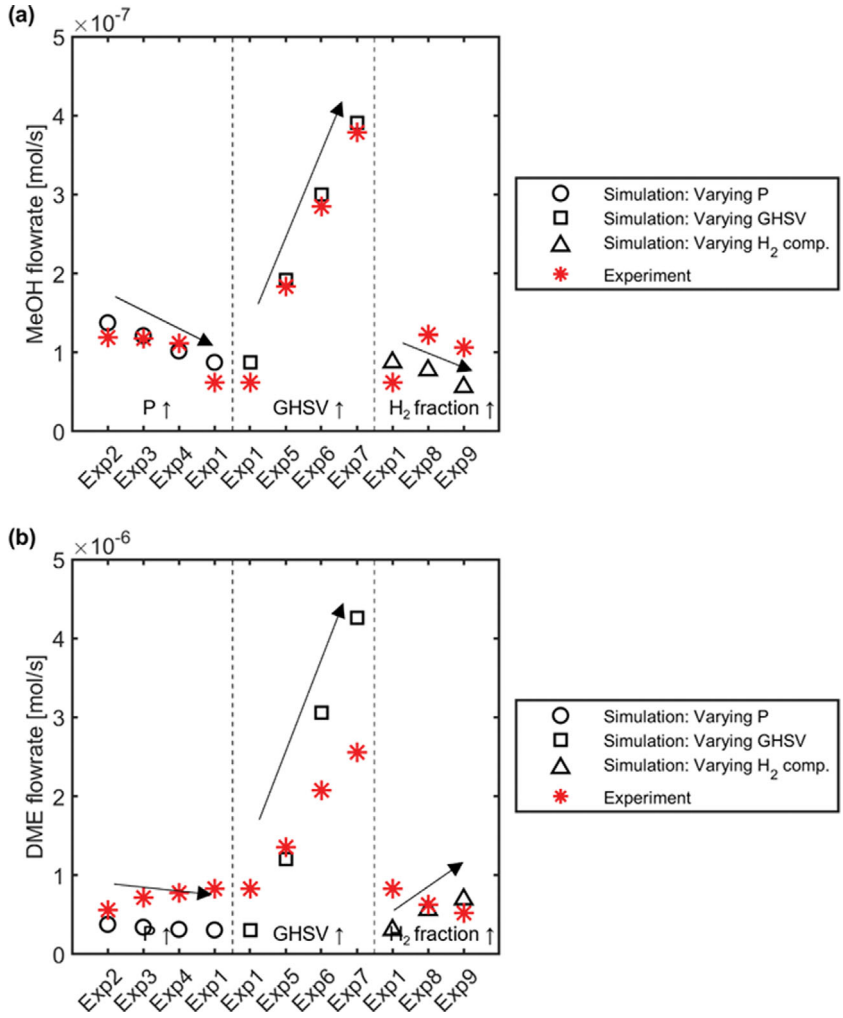

Fig. 4. Comparison of (a) MeOH flowrate [mol/s] and (b) DME flowrate [mol/s] between the simulated and experimental values. The arrangement of experiment data in x-axis shows clusters of changing in operating condition.

Note that CH_3OH* showed the lowest coverage, which is a significant difference from the results of the conventional MeOH synthesis. Low amount of MeOH on the catalytic surface indicates that the desorption of MeOH on CZA is significantly enhanced probably because the desorbed MeOH is instantly adsorbed onto the surface of FER in the shell of the hybrid catalyst.

The criterion of the major and minor components in the FER catalyst was specified to be 10^{-10} (Fig. S3 in the Supporting Information). Among the major components, the dominance of vacant sites and CH_3OH-H-Z was similar to that of the previous FER catalyst model [19], whereas the dominance of CH_3OH-CH_3OH-H-Z, related to reaction 36, showed a clear difference from the previous research [19]. In the case of the minor components, the low fraction of CH_3OCH_3-H_2O-H-Z and H_2O-CH_3-Z was the same as in the previous research [19], whereas the proportion of CH_3-Z and CH_3OCH_3-H_2O-H-Z, which were considered major components in the previous research [19], was shown to be low in this work.

Notably, reaction 31, which was determined to be a rate-determining step for the dissociative path in the reported works [19], still showed an extremely small value for H_2O-CH_3-Z, while reaction 36, which was reported to be a rate-determining step for the associative path, showed a significant increase in the value of CH_3OH-CH_3OH-H-Z, resulting from the increased MeOH concentration in the CZA/FER hybrid catalyst.

2. Reaction Rates

The kinetic parameters and reaction rates of the microkinetic model were compared with those of our previous results [19,32]. The reactions 9, 14, 19, and 28 were assumed to be at partial equilibrium in the previous work [32] to reduce the number of the parameter set of the microkinetic model [32]. Meanwhile, the partial equilibrium assumption was not applied in this work. Additionally, the gas adsorption and desorption reactions (reactions 1-6) are not to be considered in equilibrium, which differs from our previous study [32]. The CO and CO_2 adsorption (reaction 1/reaction 2) equilibrium shifted towards the forward reaction compared to the previous research [32] results, while the H_2 and MeOH adsorption equilibrium shifted towards the reverse reaction. This phenomenon is likely due to the characteristics of the CZA catalyst located in the core of the core-shell structure. The core-shell struc-

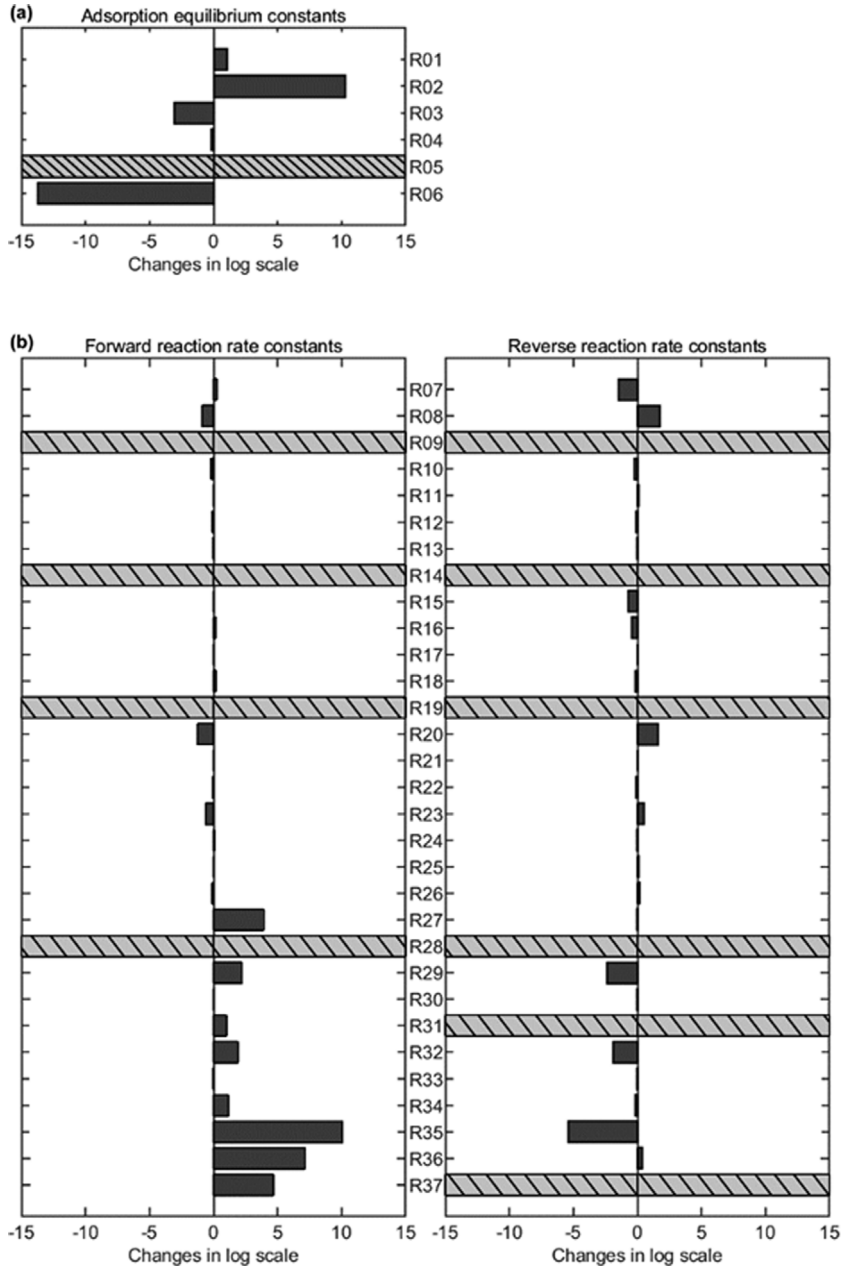

Fig. 5. Change in reaction rate constant compared to previous research[32] results (in log scale) (a) CZA adsorption reactions: Reactions 1-6 (b) CZA surface reactions and FER reactions: Reactions 7-37.

ture of CZA/FER hybrid catalyst is illustrated in Fig. 2. The gas-phase MeOH, $CH_3OH(g)$, is a product of the reaction occurring on the CZA catalyst and is generated by the desorption of CH_3OH^* (reaction 6) from the catalyst. Because the hybrid catalyst was constructed with a core-shell structure, the desorbed MeOH would be adsorbed to FER in the vicinity, resulting in the equilibrium ($CH_3OH(g)+^*\leftrightarrow CH_3OH^*$) moving to backward (more desorption).

In the case of the surface reactions, significant changes in reactions 7, 8, 20, 23, and 27 for CZA, and all surface reactions for FER were observed.

The reactions which showed significant changes were noteworthy, particularly in reactions 7 ($CO^*+O^*\leftrightarrow CO_2^*+^*$) and 20 ($CH_3O^*+H^*\leftrightarrow CH_3OH^*+^*$), which were identified as rate-determining steps (RDS) in the previous work [32]. However, in this study, reactions 20 and 27 were found to be RDS, highlighting a key factor that distinguishes the reaction rate constants at the RDS between conventional and hybrid catalysts. Additionally, reaction 8 ($CO^*+OH^*\leftrightarrow COOH^*+^*$) is a reaction that includes COOH*, which is the dominant species in this study. Reactions 23 ($HCO^*+H^*\leftrightarrow CH_2O^*+^*$) and 27 ($CH_3O^*+HCO^*\leftrightarrow CH_3OH^*+CO^*$) are related to the surface component HCO* and reaction 26 ($CH_3O^*+CO^*\leftrightarrow CH_2O^*+HCO^*$), which was treated as the RDS in previous research [32]. In comparison to the previous research [32], reaction 7 ($CO^*+O^*\leftrightarrow CO_2^*+^*$) shifted towards the forward while reac-

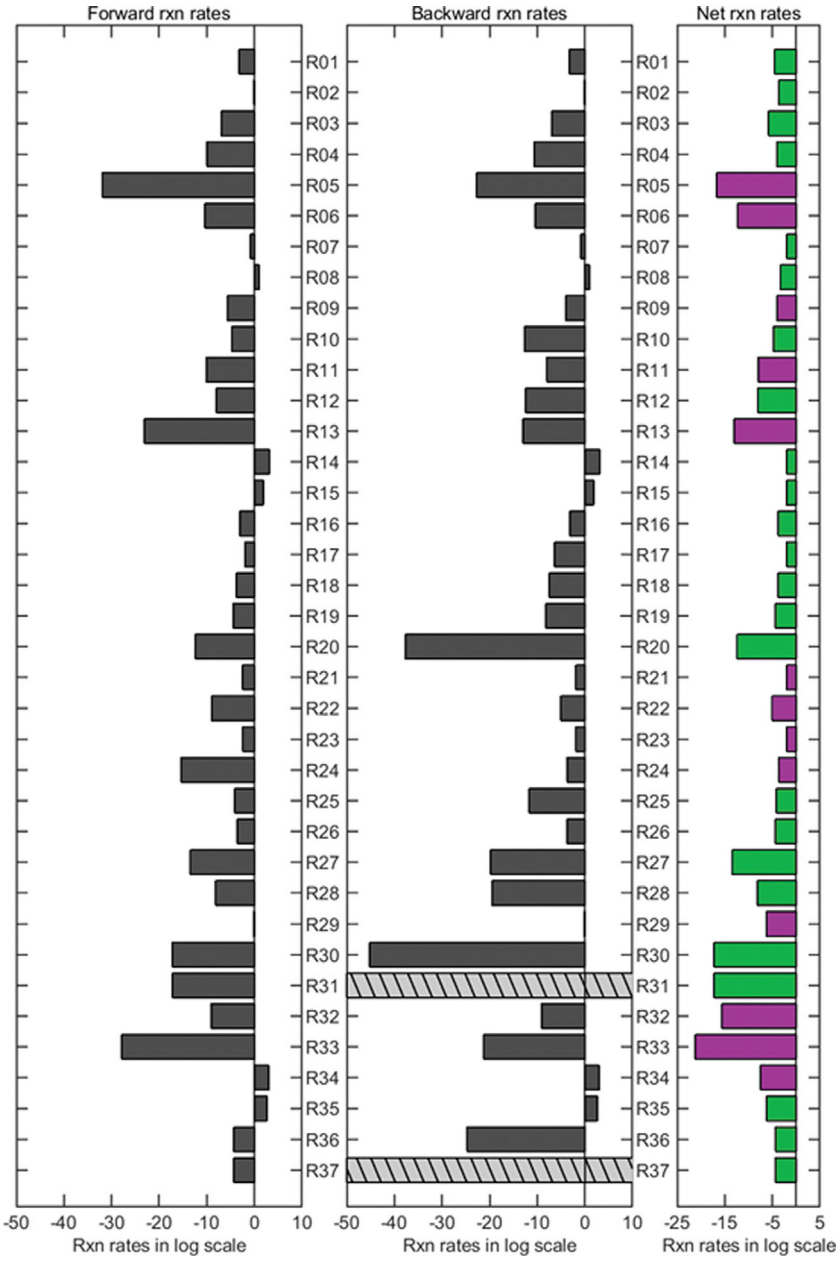

Fig. 6. Forward, backward and net reaction rates using estimated parameter set in operating condition of Exp1: Base case (in log scale). The green color means the value in log is positive and the purple means the value in log is negative.

tion 8 (CO*+OH*↔COOH*+*) shifted backwards. This shift implies that the conversion of CO* to CO_2* over the hybrid catalyst increased in the direct path (reaction 7) and decreased in the indirect path (reactions 8-9) than previous work [32].

In addition, the shift of reaction 20 (CH_3O*+H*↔CH_3OH*+*) towards backward suggests that reaction 27 (CH_3O*+HCO*↔ CH_3OH*+CO*) might provide an alternative pathway for producing MeOH* over the hybrid catalyst. Moreover, the changes in the parameters of reactions 20, 23, and 27 indicate that HCO* could become a key intermediate over the hybrid catalyst.

It is also necessary to examine the reaction rates to observe the reaction behavior. Fig. 6 displays the forward, backward, and net reaction rates of each reaction calculated under the operating conditions of Exp1 (base case). In the net reaction rates chart on the right-hand side of Fig. 6, the green color indicates a positive reaction rate, while purple indicates a negative reaction rate.

In Fig. 6, the log-scaled reaction rates of the base case are presented. Apart from reaction 5 (CH_2O (g)+*↔CH_2O*), the forward and reverse reaction rates of reactions 1-6, 29, 32, and 35, which are gas adsorption/desorption reactions, are equal, indicating that adsorption and desorption reactions have reached equilibrium. For reaction 5, the gas component CH_2O(g) has a low concentration of approximately 10^{-18} mol/m^3, the reaction is rate-determining, although it is not found to have a significant effect on the overall system based on Campbell's degree of rate control analysis [39-41]. In the surface reactions over CZA, reactions 7-9, 14-19,

and 21-26 were particularly fast in the system. As for the reaction that is commonly considered the rate-controlling step, reaction 20 ($CH_3O^*+H^* \leftrightarrow CH_3OH^*+^*$), it was also found to be a very slow reaction in this study, consistent with previous research [32]. However, reaction 27 ($CH_3O^*+HCO^* \leftrightarrow CH_3OH^*+CO^*$) was found to have a higher forward rate compared to previous studies, as shown in Fig. 5. This is believed to be due to the equilibrium of reaction 6 ($CH_3OH(g)+^* \leftrightarrow CH_3OH^*$) shifting towards the desorption reaction ($CH_3OH^* \rightarrow CH_3OH(g)+^*$) compared to previous studies, which helps to alleviate the bottleneck effect of the CH_3OH^* shortage. Before moving on to the reaction on the FER catalyst, we examined the reaction rates of reactions 9, 14, 19, and 28 that were excluded from the system in previous studies due to the assumption of partial equilibrium. As they all correspond to relatively fast reactions in the system, the assumption of partial equilibrium was appropriate. Furthermore, the forward reactions were favored in reaction 8 ($CO^*+OH^* \leftrightarrow COOH^*+^*$), which is the fastest reaction producing COOH*. This result is consistent with COOH* being identified as one of the major surface components.

As the result shown by Fig. 6, the main path of the CO conversion to CO_2 via HCO* and HCOO** is followed.

via COOH*: forward reaction of reaction 8 ($CO^*+OH^* \leftrightarrow COOH^*+^*$) and reverse reaction of reaction 9 ($COOH^*+^* \leftrightarrow CO_2^*+H^*$).

Also, the CO conversion to MeOH via HCO*, CH_2O^* and CH_3O^* is followed.

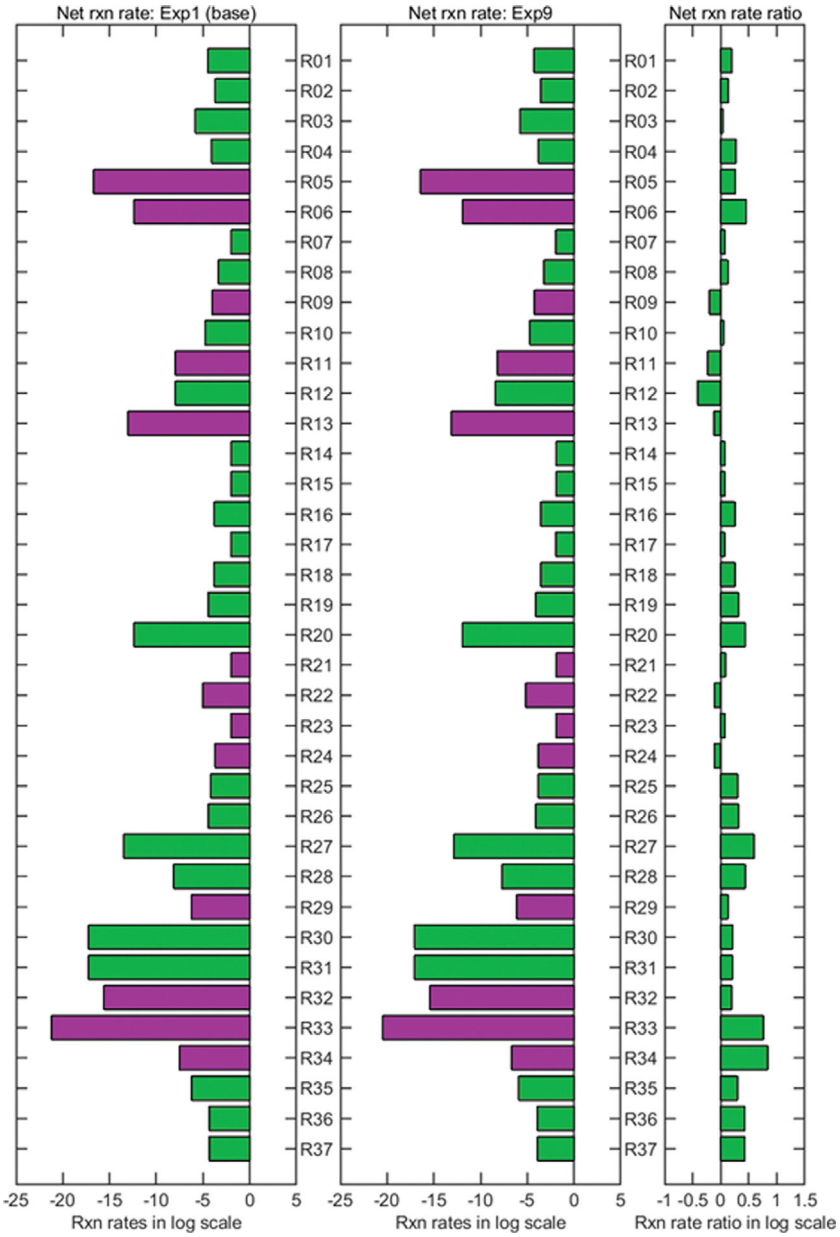

Fig. 7. Ratio of the forward, backward and net reaction rates in the Exp9: High H_2 composition in feed case to those in the base case (in log scale). The green color means the value in log is positive and purple means the value in log is negative.

Forward reaction of reaction 25 ($CO^*+H_2O^* \leftrightarrow HCO^*+OH^*$), reverse reaction of reaction 26 ($CH_2O^*+HCO^* \leftrightarrow CH_3O^*+CO^*$), forward reaction of reaction 20 ($CH_3O^*+H^* \leftrightarrow CH_3OH^*+^*$), forward reaction of reaction 27 ($CH_3O^*+HCO^* \leftrightarrow CH_3OH^*+CO^*$).

Finally, the CO_2 conversion to MeOH via HCOO** is followed.

Forward reaction of reaction 14 ($CO_2^*+H^* \leftrightarrow HCOO^{**}$), forward reaction of reaction 15 ($HCOO^{**}+H^* \leftrightarrow H_2COO^*+2^*$), forward reaction of reaction 17 ($H_2COO^*+H^* \leftrightarrow CH_2O^*+O^*$), forward reaction of reaction 19 ($CH_2O^*+H^* \leftrightarrow CH_3O^*+^*$), forward reaction of reaction 20 ($CH_3O^*+H^* \leftrightarrow CH_3OH^*+O^*$).

Moving on to the FER catalyst reactions (reactions 29-37), a brief review reveals that the reaction rates of MeOH adsorption reactions, specifically reactions 29, 32, and 35, increased in this system where MeOH diffusion was promoted. Moreover, it can be seen that the associative path, reactions 35-37, was accelerated more than the dissociative path, reactions 29-34.

To further investigate the effects of hydrogen concentration on CO_2 conversion, the reaction rates under high hydrogen composition in feed condition, Exp9, were compared with the base case, Exp1.

The reaction rates were investigated under high H_2 composition in feed conditions where CO_2 conversion occurs. Fig. 7 shows the reaction rate difference in log scale between the Exp1 (base case) and Exp9. Reactions 20 and 27, the main reactions of CZA which produce CH_3OH^*, increased in Exp9 than Exp1, which causes increasing MeOH production over CZA. As the production of MeOH over CZA increased, the MeOH adsorption to FER, the reaction rates of reaction 29, 32 and 35 also increased. This resulted in that even if the MeOH production over CZA increased in Exp9 than Exp1, the adsorption reactions, reactions 6, 29, 32 and 35 also were getting faster, so that the overall MeOH production rate decreased, which is shown in Fig. 4. The reaction rate of reactions 8 ($CO^*+OH^* \leftrightarrow COOH^*+^*$) slightly increased, as contrasted with the reaction rates of reaction 9 ($CO_2^*+H^* \leftrightarrow COOH^*+^*$) decreased, indicating the equilibrium of reaction 9, which has H* as a reactant, moved to forward in increase of H_2 composition in feed (Exp9). The result for the reaction 14-19 indicates an accelerated rate of the CO_2 hydrogenation pathway under conditions of high H_2 composition. This aligns well with the positive conversion of CO_2 observed in Exp8 and Exp9, where the feed condition had a high H_2 composition. As Fig. S2 (site fraction over CZA in supporting information) shows, the site fraction of CO* increased and the vacant site fraction decreased in Exp9 than Exp1. The reactions related with producing CH_3OH^* are reactions 19-20 and 26-28 and those show getting faster with Exp9 condition in Fig. 7. The increase of CH_3OH^* results in a shift in the equilibrium point of reaction 6 towards the desorption reaction, thereby generating a similar effect to increasing the partial pressure of MeOH near the FER catalyst. This, in turn, triggers MeOH clustering, which can speed up the associative pathway [2]. Last, HCOO** can be further investigated with the result in Fig. 7. The surface component HCOO** is related to reaction 14 and reaction 15, each is a part of H_2 hydrogenation, which are increased in Exp9, in high H_2 composition in feed condition. The studies suggesting HCOO** [6,9] are important or are related with the CO_2 conversion, were results from relatively high H_2 composition in feed condition, as similar

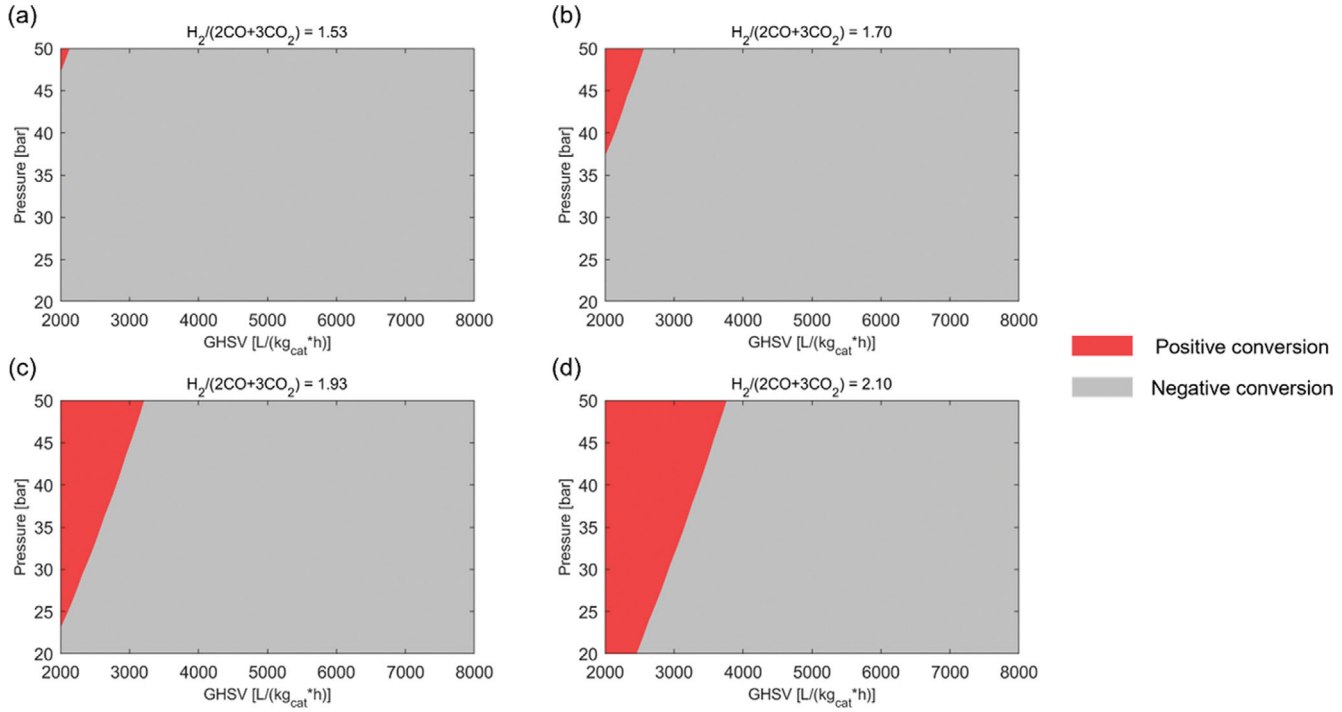

Fig. 8. Case study result: Analysis of the area where CO_2 conversion occurs when the GHSV and pressure conditions are changed at specific H_2 composition in feed condition values, (a) $H_2/(2CO+3CO_2)$=1.53 (b) $H_2/(2CO+3CO_2)$=1.70 (c) $H_2/(2CO+3CO_2)$=1.93 (d) $H_2/(2CO+3CO_2)$=2.10. The red area represents the region where CO_2 consumption occurs, while the gray area indicates the region where CO_2 generation occurs.

as this study.

Note that the tendency of models in predicting DME production rates did not match with experimental values under increasing the H_2 composition in feed condition, Exp1 and 8-9. It would be due to limitations in the model's ability to capture the complexities of the catalytic system. It might exaggerate the effect of the increase in reaction rates of reactions 19 and 20 on CH_3OH* production and the consequent promotion of the adsorption reactions for MeOH over FER (reactions 29, 32, and 35) in the modeling, or it could also result from experimental error.

3. Case Study: Converting CO_2 into MeOH and DME

Examining the experimental results shows that the CO_2 conversion was represented in cases with high H_2 composition in the feed. In most cases, negative CO_2 conversion was shown, meaning the generation of CO_2, but in experimental runs 8 and 9, with two high H_2 composition in feed conditions from all nine experimental runs, positive CO_2 conversion was shown, meaning the consumption and conversion of CO_2. Based on these experimental results, a case study was performed to find the region that represents positive CO_2 conversion through reproducing the results in a model. The calculation of a total of 27,000 points for case studies was performed based on 30 points interpolation for each variable, while the ratio of CO and CO_2 in the feed was fixed within the experimental conditions of temperature 250 °C, pressure 20-50 bar, GHSV 2,000-8,000 L/(kg_{cat} h), and $H_2/(2CO+3CO_2)$ value range of 0.96-2.1.

According to the case study results in Fig. 8, CO_2 consumption can occur at lower pressures and higher GHSV values as the $H_2/(2CO+3CO_2)$ value increased, but when the GHSV value exceeded 4000, CO_2 was produced at all the pressure and GHSV. Since high GHSV values are required for high productivity, it appears that there is a trade-off between CO_2 conversion and productivity. To convert CO_2 at high GHSV, higher $H_2/(2CO+3CO_2)$ values and higher pressure are required, which is not recommended operating conditions.

CONCLUSION

The CZA/FER hybrid catalyst was designed with a core-shell structure to effectively adsorb MeOH, an important intermediate in the DME path, onto the FER. Our previous research confirmed the benefits of MeOH and DME productivity through lumped kinetic modeling, but it was difficult to understand how each single-step reaction was promoted. In this study, a microkinetic model consisting of a total of 72 reactions, including 35 reversible reactions and two irreversible reactions, was constructed to verify whether the catalyst promotes MeOH diffusion to FER as intended. Parameter estimation was conducted to enable the model to predict a total of nine experimental data. The microkinetic model for the CZA/FER hybrid catalyst developed by our research team is significant in that it was created without any assumptions. The model, which consists of 72 reactions, was constructed without applying various assumptions, such as adsorption equilibrium and surface reaction equilibrium, and was able to predict experimental results within the range of experimental conditions without any uninterpretable points, even at different reaction rate scales between the two catalysts. This is noteworthy because it shows that a model can be created to predict experimental values without assumptions, which is a major achievement.

Based on the constructed model, the parameters of each reaction were analyzed, and it was confirmed that the major components of site coverage on the CZA surface and FER zeolite surface were five and three components in each, respectively. Additionally, information on the rate-determining step and competitive relationship between associative and dissociative paths was obtained. Unlike the existing FER-only system, the associative path was dominant due to the hybridization of catalyst, causing an increase of effective MeOH concentration. Finally, through a case study, it was possible to confirm the operating conditions for CO_2 conversion, which provides an important guideline for preparing for the increase in operating cost due to carbon taxes in the petrochemical process. If further research is conducted based on the results of the model developed in this study, the economic efficiency of the syngas to DME process can be improved.

ACKNOWLEDGEMENT

This research was supported by the C1 Gas Refinery Program through the National Research Foundation of Korea (NRF), funded by the Ministry of Science, ICT & Future Planning (NRF-2021M3 D3A1A01022109).

SUPPORTING INFORMATION

Additional information as noted in the text. This information is available via the Internet at http://www.springer.com/chemistry/journal/11814.

REFERENCES

1. B. Hamed and A. Chad, *Catal. Ind.*, **11**(1), 7 (2019).
2. J. R. Di Iorio, A. J. Hoffman, C. T. Nimlos, S. Nystrom, D. Hibbitts and R. Gounder, *J. Catal.*, **380**, 161 (2019).
3. A. Brunetti, M. Migliori, D. Cozza, E. Catizzone, G. Giordano and G. Barbieri, *ACS Sustain. Chem. Eng.*, **8**(28), 10471 (2020).
4. A. Trypolskyi, A. Zhokh, V. Gritsenko, M. Chen, J. Tang and P. Strizhak, *Chem. Papers*, **75**(7), 3429 (2021).
5. A. A. Rownaghi, F. Rezaei and J. Hedlund, *Micropor. Mesopor. Mater.*, **151**, 26 (2012).
6. L. C. Grabow and M. Mavrikakis, *ACS Catal.*, **1**(4), 365 (2011).
7. A. T. Aguayo, J. Ereña, D. Mier, J. M. Arandes, M. Olazar and J. Bilbao, *Ind. Eng. Chem. Res.*, **46**(17), 5522 (2007).
8. S. Fujita, S. Moribe, Y. Kanamori, M. Kakudate and N. Takezawa, *Appl. Catal. A Gen.*, **207**(1), 121 (2001).
9. Y. H. Lim, M. Y. Gim, H. Kim and D. H. Kim, *Fuel Process. Technol.*, **227**, 107107 (2022).
10. J. Park, Y. Woo, H. S. Jung, H. Yang, W. B. Lee, J. W. Bae and M.-J. Park, *Catal. Today*, **388-389**, 323 (2022).
11. J. Skrzypek, M. Lachowska and H. Moroz, *Chem. Eng. Sci.*, **46**(11), 2809 (1991).
12. G. H. Graaf, *The synthesis of methanol in gas-solid and gas-slurry reactors*, Ph. D. dissertation, Dept. Math. & Nat. Sci. Univ. Groningen, The Netherlands (1988).

13. G. H. Graaf, E. J. Stamhuis and A. A. C. M. Beenackers, *Chem. Eng. Sci.*, **43**(12), 3185 (1988).
14. G. H. Graaf, H. Scholtens, E. J. Stamhuis and A. A. C. M. Beenackers, *Chem. Eng. Sci.*, **45**(4), 773 (1990).
15. G. H. Graaf, P. J. J. M. Sijtsema, E. J. Stamhuis and G. E. H. Joosten, *Chem. Eng. Sci.*, **41**(11), 2883 (1986).
16. S. Svelle, S. Kolboe, U. Olsbye and O. Swang, *J. Phys. Chem. B*, **107**(22), 5251 (2003).
17. P. G. Moses and J. K. Nørskov, *ACS Catal.*, **3**(4), 735 (2013).
18. H. Xin, X. Li, Y. Fang, X. Yi, W. Hu, Y. Chu, F. Zhang, A. Zheng, H. Zhang and X. Li, *J. Catal.*, **312**, 204 (2014).
19. J. Park, J. Cho, M.-J. Park and W. B. Lee, *Catal. Today*, **375**, 314 (2021).
20. A. H. Motagamwala and J. A. Dumesic, *Chem. Rev.*, **121**(2), 1049 (2021).
21. A. Ghorbanpour, J. D. Rimer and L. C. Grabow, *ACS Catal.*, **6**(4), 2287 (2016).
22. C. Karakaya, H. Zhu and R. J. Kee, *Chem. Eng. Sci.*, **123**, 474 (2015).
23. C. Karakaya, S. H. Morejudo, H. Zhu and R. J. Kee, *Ind. Eng. Chem. Res.*, **55**(37), 9895 (2016).
24. A. Baz and A. Holewinski, *J. Catal.*, **384**, 1 (2020).
25. F. Figueras, A. Nohl, L. de Mourgues and Y. Trambouze, *Trans. Faraday Soc.*, **67**, 1155 (1971).
26. L. Kubelkov, J. Novákov and K. Nedomov, *J. Catal.*, **124**(2), 441 (1990).
27. S. R. Blaszkowski and R. A. van Santen, *J. Phys. Chem.*, **99**(30), 11728 (1995).
28. S. R. Blaszkowski and R. A. Van Santen, *J. Am. Chem. Soc.*, **118**(21), 5152 (1996).
29. A. J. Jones, S. I. Zones and E. Iglesia, *J. Phys. Chem. C*, **118**(31), 17787 (2014).
30. A. J. Jones and E. Iglesia, *Angew. Chem. Int. Ed.*, **53**(45), 12177 (2014).
31. R. T. Carr, M. Neurock and E. Iglesia, *J. Catal.*, **278**(1), 78 (2011).
32. J. Park, J. Cho, Y. Lee, M.-J. Park and W. B. Lee, *Ind. Eng. Chem. Res.*, **58**(20), 8663 (2019).
33. R. D. Cortright and J. A. Dumesic, *Adv. Catal.*, **46**, 161 (2001).
34. E. Shustorovich and H. Sellers, *Surf. Sci. Rep.*, **31**(1), 1 (1998).
35. G. Hetzer, P. Pulay and H.-J. Werner, *Chem. Phys. Lett.*, **290**(1), 143 (1998).
36. T. Tagawab, G. Pleizier and Y. Amenomiya, *Appl. Catal.*, **18**(2), 285 (1985).
37. A. A. Gokhale, J. A. Dumesic and M. Mavrikakis, *J. Am. Chem. Soc.*, **130**(4), 1402 (2008).
38. N. Park, M.-J. Park, Y.-J. Lee, K.-S. Ha and K.-W. Jun, *Fuel Process. Technol.*, **125**, 139 (2014).
39. C. T. Campbell, *ACS Catal.*, **7**(4), 2770 (2017).
40. C. T. Campbell, *J. Catal.*, **204**(2), 520 (2001).
41. C. T. Campbell, *Top. Catal.*, **1**(3), 353 (1994).

Supporting Information

Microkinetic study of syngas conversion to dimethyl ether over a bifunctional catalyst: CZA/FER

Jiyeong Cho*, Jongmin Park*, Hyun Seung Jung, Jong Wook Bae**, Jonggeol Na***,†, Won Bo Lee*,† and Myung-June Park****,†**

*School of Chemical and Biological Engineering, Institute of Chemical Processes, Seoul National University, Gwanak-ro 1, Gwanak-gu, Seoul 08826, Korea
**School of Chemical Engineering, Sungkyunkwan University (SKKU), Suwon 16419, Korea
***Department of Chemical Engineering and Materials Science, Graduate Program in System Health Science and Engineering, Ewha Womans University, Seoul 03760, Korea
****Department of Chemical Engineering, Ajou University, Suwon 16499, Korea
(*Received 17 June 2023 • Revised 7 July 2023 • Accepted 10 July 2023*)

Fig. S1 shows a parity plot of the microkinetic model developed in this study. The plot consists of 36 points, with nine points for each of the following parameters: CO conversion, CO_2 conversion, MeOH flowrate, and DME flowrate. Each element of the plot is normalized using the mean and standard deviation of the experimental data. Table S1 contains the raw and normalized data for the CO conversion, CO_2 conversion, MeOH flowrate, and DME flowrate obtained from both experiments and the model.

Fig. S2 and S3 present the site fractions obtained from the microkinetic model simulation, with the corresponding raw data included in Tables S2 and S3, respectively.

The site fractions over CZA are depicted in Fig. S2, where the major and minor components were determined based on the criterion of 10^{-8}. The major components, which are greater than 10^{-8}, are displayed in (a), while the minor components, which are less than 10^{-8}, are shown in (b).

In Fig. S3, the site fractions over FER are shown. The major and minor components were determined using the criterion of 10^{-10}. The major components, which are greater than 10^{-10}, are displayed in (a), while the minor components, which are less than 10^{-10}, are shown in (b).

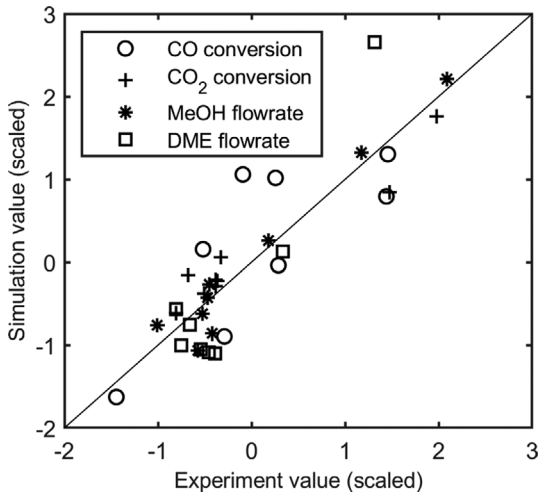

Fig. S1. Parity plot made by scaled with nomalizing elements in objective function of developed microkinetic model.

Table S1. The raw data and normalized data of CO conversion, CO_2 conversion, MeOH flowrate and DME flowrate of experiments and calculated by model

		Exp1	Exp2	Exp3	Exp4	Exp5	Exp6	Exp7	Exp8	Exp9	Mean	Std. Dev.
CO conversion [%]	Exp	88.60	69.50	80.90	88.50	75.60	77.10	71.80	78.40	80.70	79.01	6.21
	Model	87.59	68.30	78.76	84.24	80.04	73.11	65.38	85.98	85.71	-	-
CO_2 conversion [%]	Exp	−18.00	−29.00	−22.10	−26.00	−18.80	−19.20	−19.30	23.30	34.80	−10.48	21.58
	Model	−9.06	−24.51	−19.15	−14.00	−15.69	−17.00	−15.36	8.77	29.76	-	-
MeOH flowrate [10^{-8} mol/s]	Exp	6.187	11.92	11.75	11.16	18.38	28.49	37.86	12.25	10.64	16.52	9.63
	Model	8.742	13.76	12.12	10.19	19.20	30.02	39.09	7.746	5.611	-	-
DME flowrate [mol/s]	Exp	8.267	5.622	7.144	7.772	13.57	20.79	25.54	6.261	5.183	11.13	6.93
	Model	33.067	3.774	3.420	3.145	12.08	30.63	42.59	5.592	6.949	-	-
CO conversion [Normalized]	Exp	1.545	−1.533	0.304	1.529	−0.550	−0.308	−1.162	−0.098	0.272	-	-
	Model	1.383	−1.726	−0.040	0.842	0.165	−0.950	−2.197	1.123	1.079	-	-
CO_2 conversion [Normalized]	Exp	−0.349	−0.858	−0.539	−0.719	−0.386	−0.404	−0.409	1.565	2.098	-	-
	Model	0.066	−0.650	−0.402	−0.163	−0.242	−0.302	−0.226	0.892	1.865	-	-
MeOH flowrate [Normalized]	Exp	−1.073	−0.450	−0.466	−0.524	0.183	1.173	2.090	−0.418	−0.575	-	-
	Model	−0.808	−0.287	−0.456	−0.657	0.279	1.403	2.345	−0.911	−1.133	-	-
DME flowrate [Normalized]	Exp	−0.413	−0.795	−0.575	−0.484	0.352	1.395	2.081	−0.703	−0.858	-	-
	Model	−1.164	−1.062	−1.113	−1.153	0.137	2.816	4.543	−0.799	−0.603	-	-

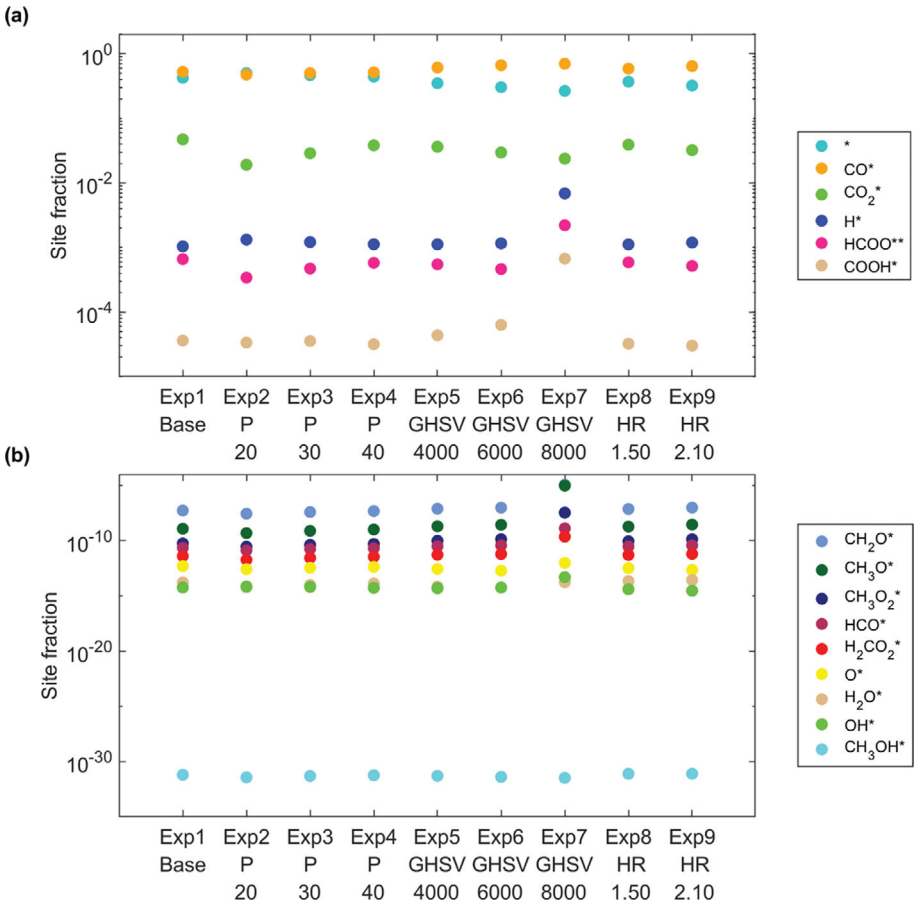

Fig. S2. Site fraction based on the result of the simulation using microkinetic model: site fraction on CZA. HR means the hydrogen ratio=H_2/(2CO+3CO_2) in feed. (a) major components: site fractions that are greater than 10^{-8} (b) minor components: site fractions that are less than 10^{-8}.

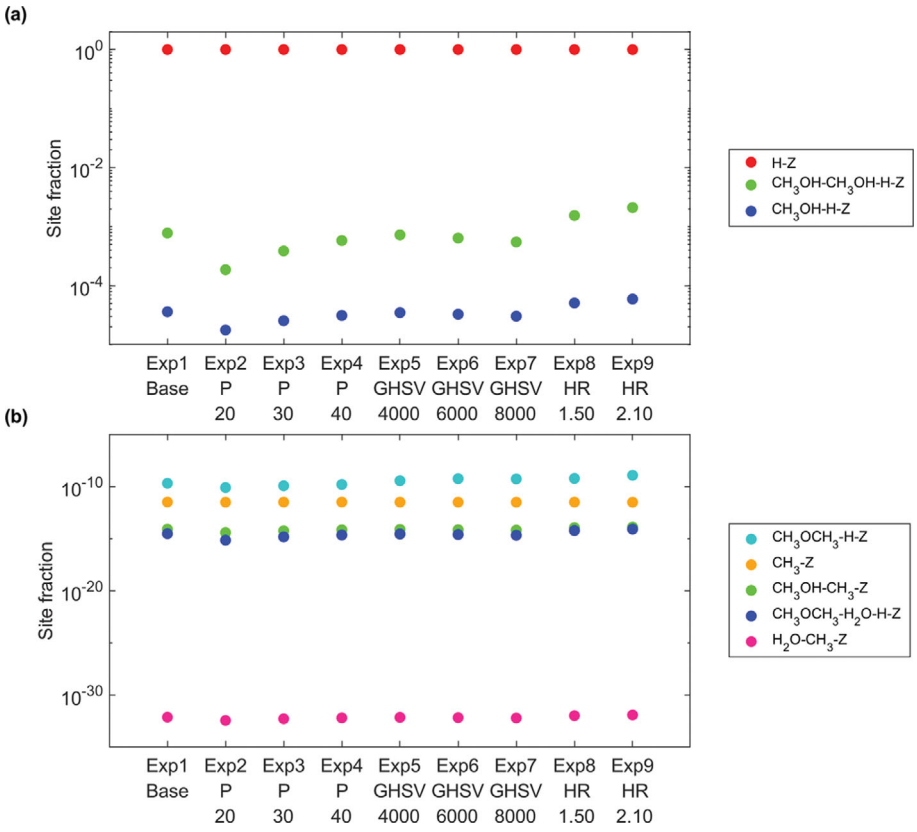

Fig. S3. Site fraction based on the result of the simulation using microkinetic model: site fraction on FER. HR means the hydrogen ratio=H_2/(2CO+3CO_2) in feed. (a) major components: site fractions that are greater than 10^{-10} (b) minor components: site fractions that are less than 10^{-10}.

Table S2. Site fraction based on the result of the simulation using microkinetic model: site fractions on CZA

Component	Exp1	Exp2	Exp3	Exp4	Exp5	Exp6	Exp7	Exp8	Exp9
* (vacant)	4.254E-01	5.032E-01	4.665E-01	4.431E-01	3.499E-01	3.037E-01	2.655E-01	3.693E-01	3.218E-01
CO*	5.256E-01	4.760E-01	5.029E-01	5.170E-01	6.121E-01	6.650E-01	7.010E-01	5.899E-01	6.443E-01
CO_2*	4.721E-02	1.911E-02	2.884E-02	3.822E-02	3.626E-02	2.956E-02	2.377E-02	3.906E-02	3.217E-02
H*	1.037E-03	1.323E-03	1.212E-03	1.120E-03	1.118E-03	1.159E-03	6.882E-03	1.116E-03	1.192E-03
HCOO**	6.614E-04	3.414E-04	4.719E-04	5.781E-04	5.476E-04	4.627E-04	2.210E-03	5.888E-04	5.178E-04
COOH*	3.614E-05	3.368E-05	3.555E-05	3.167E-05	4.358E-05	6.326E-05	6.715E-04	3.237E-05	3.014E-05
CH_2O*	5.504E-08	2.833E-08	4.002E-08	4.892E-08	7.990E-08	1.002E-07	1.155E-05	7.528E-08	1.009E-07
CH_3O	1.236E-09	4.948E-10	7.865E-10	1.045E-09	2.049E-09	2.798E-09	9.588E-06	1.919E-09	2.934E-09
CH_3O_2*	5.711E-11	2.891E-11	4.209E-11	5.150E-11	9.880E-11	1.370E-10	3.530E-08	9.002E-11	1.364E-10
HCO*	2.309E-11	1.372E-11	1.786E-11	2.096E-11	3.182E-11	3.833E-11	1.329E-09	3.029E-11	3.857E-11
H_2CO_2*	4.070E-12	1.912E-12	2.817E-12	3.540E-12	5.371E-12	6.240E-12	2.349E-10	5.175E-12	6.400E-12
O*	5.022E-13	2.688E-13	3.551E-13	4.328E-13	2.859E-13	1.953E-13	9.846E-13	3.333E-13	2.302E-13
H_2O*	1.707E-14	6.140E-15	1.004E-14	1.364E-14	7.080E-15	5.697E-15	1.738E-14	2.231E-14	2.832E-14
OH*	5.889E-15	7.174E-15	6.643E-15	5.466E-15	5.015E-15	5.818E-15	5.088E-14	4.080E-15	3.030E-15
CH_3OH*	6.383E-32	3.701E-32	4.943E-32	5.750E-32	5.065E-32	4.132E-32	3.331E-32	7.816E-32	7.947E-32

Table S3. Site fraction based on the result of the simulation using microkinetic model: site fractions on FER

Component	Exp1	Exp2	Exp3	Exp4	Exp5	Exp6	Exp7	Exp8	Exp9
H-Z	9.992E-01	9.998E-01	9.996E-01	9.994E-01	9.992E-01	9.993E-01	9.994E-01	9.984E-01	9.978E-01
CH_3OH-CH_3OH-H-Z	7.793E-04	1.870E-04	3.884E-04	5.830E-04	7.257E-04	6.409E-04	5.507E-04	1.550E-03	2.110E-03
CH_3OH-H-Z	3.615E-05	1.772E-05	2.553E-05	3.127E-05	3.489E-05	3.279E-05	3.039E-05	5.096E-05	5.944E-05
CH_3OCH_3-H-Z	1.981E-10	7.740E-11	1.154E-10	1.511E-10	3.485E-10	5.436E-10	5.122E-10	5.716E-10	1.148E-09
CH_3-Z	3.115E-12	3.002E-12	3.065E-12	3.112E-12	3.043E-12	3.017E-12	2.996E-12	3.067E-12	2.986E-12
CH_3OH-CH_3-Z	7.778E-15	3.671E-15	5.402E-15	6.720E-15	7.332E-15	6.831E-15	6.287E-15	1.080E-14	1.227E-14
CH_3OCH_3-H_2O-H-Z	2.889E-15	6.935E-16	1.440E-15	2.162E-15	2.691E-15	2.376E-15	2.042E-15	5.747E-15	7.822E-15
H_2O-CH_3-Z	7.444E-33	3.648E-33	5.257E-33	6.439E-33	7.184E-33	6.752E-33	6.259E-33	1.049E-32	1.224E-32